J Nanopart Res (2013) 15:1815
DOI 10.1007/s11051-013-1815-y

RESEARCH PAPER

Mechanisms of nanoclay-enhanced plastic foaming processes: effects of nanoclay intercalation and exfoliation

Anson Wong · Stephan F. L. Wijnands · Takashi Kuboki · Chul B. Park

Received: 14 April 2013 / Accepted: 19 June 2013 / Published online: 10 July 2013

Abstract The foaming behaviors of high-density polypropylene–nanoclay composites with intercalated and exfoliated nanoclay particles blown with carbon dioxide were examined via in situ observation of the foaming processes in a high-temperature/high-pressure view-cell. The intercalated nanoclay particles were 300–600 nm in length and 50–200 nm in thickness, while the exfoliated nanoclay particles were 100–200 nm in length and 1 nm in thickness. Contrary to common belief, it was discovered that intercalated nanoclay yielded higher cell density than exfoliated nanoclay despite its lower particle density. This was attributed to the higher tensile stresses generated around the larger and stiffer intercalated nanoclay particles, which led to increase in supersaturation level for cell nucleation. Also, the coupling agent used to exfoliate nanoclay would increase the affinity between polymer and surface of nanoclay particles. Consequently, the critical work needed for cell nucleation would be increased; pre-existing microvoids, which could act as seeds for cell nucleation, were also less likely to exist. Meanwhile, exfoliated nanoclay had better cell stabilization ability to prevent cell coalescence and cell coarsening. This investigation clarifies the roles of nanoclay in plastic foaming processes and provides guidance for the advancement of polymer nanocomposite foaming technology.

Keywords High-density polypropylene · Foam · Exfoliated nanoclay · Intercalated nanoclay · Carbon dioxide · Foaming visualization

A. Wong · S. F. L. Wijnands · T. Kuboki · C. B. Park (✉)
Microcellular Plastics Manufacturing Laboratory, Department of Mechanical & Industrial Engineering, University of Toronto, Toronto, ON M5S 3G8, Canada
e-mail: park@mie.utoronto.ca

S. F. L. Wijnands
Eindhoven University of Technology, Den Dolech 2, 5612 AZ Eindhoven, The Netherlands

Introduction

Foamed plastics with a high cell density offer superior mechanical properties such as higher impact strength (Matuana et al. 1997; Shimbo et al. 2007) and fatigue life (Seeler and Kumar 1993), as well as better thermal and acoustic insulation properties (Suh et al. 2000; Shimbo et al. 1992), when compared to their solid counterparts. To achieve this, many researchers have investigated the foamability of plastics with a wide range of cell-nucleating agents [e.g., talc (Xu et al. 2003; Wong and Park 2012), calcium carbonate (Yang and Han 1984), and zinc stearate (Colton and Suh 1987a, b; Yang and Han 1984)] to identify effective cell-nucleating agents and their characteristics. Currently, micron-sized cell-nucleating agents are widely used in plastic foaming industry to promote cell nucleation for the production of fine-cell and/or

microcellular foams. In recent years, nanoclay has drawn significant research interests as nucleating agents in plastic foaming owing to their small sizes and high aspect ratios; hence, high particle density and large interfacial surface area for heterogeneous nucleation. Okamoto et al. (2001) and Taki et al. (2004) investigated foaming of polypropylene (PP)–nanoclay composites with CO_2, and they demonstrated that cell density increased as the nanoclay loading increased (up to 7.5 wt%). Similar results were obtained by Zheng et al. (2010) in a PP-nanoclay extrusion foaming study. Meanwhile, Lee et al. (2007b) demonstrated that the optimal loading of nanoclay to achieve maximum cell density in low density polyethylene (LDPE)–nanoclay foams was lower than 1 wt%. They attributed the decrease in cell density to the insufficient dispersion of nanoclay at high loadings that caused decrease in interfacial area for heterogeneous nucleation. To be specific, nanoclay particles naturally appear as layered stacks of platelets consisting of two silica tetrahedral fused to an edge-shared octahedral sheet of aluminum or magnesium hydroxide (Giannelis 1996). In order to generate a uniform dispersion of nanoclay in plastic (i.e., an exfoliated nanoclay plastic composite) by extrusion compounding, nanoclay platelets needs to be delaminated by sufficient shear forces so that individual platelets could be separated and uniformly distributed in the polymer matrix. To achieve this, strong interfacial interaction between the polymer matrix and nanoclay particles is needed. This could be achieved easily with highly polar plastics such as polyamides (Usuki et al. 1993). However, many commodity plastics used in industries are nonpolar or weakly polar polymers (e.g., polyethylene, polypropylene, and polystyrene), so they have weak interactions with nanoclay. Therefore, it is difficult to achieve complete exfoliation of nanoclay platelets in many plastic/nanoclay nanocomposites (Tanoue et al. 2004; Ton-That et al. 2004). In many cases, nanoclay composites with these plastics are intercalated nanocomposites in which the nanoclay particles exist largely in layered stacks. Consequently, the particle density and interfacial area for heterogeneous cell nucleation for the intercalated case would be lower than the exfoliated case. This reason was given by Lee et al. (2007b) to explain the higher cell density of LDPE–nanoclay composites foams with exfoliated nanoclay as compared to those with intercalated nanoclay.

While these studies have led to valuable insights on the effect of nanoclay on plastic foaming behavior, the final conclusions on the optimal nanoclay content varied from one study to another. This could be due to the different degrees of exfoliation of nanoclay within the plastic nanocomposites in these studies; hence, the effect of nanoclay content could not be examined in an isolated manner. In this context, a fundamental understanding on the effects of exfoliation of nanoclay on cell nucleation and growth behavior is imperative to the effective usage of nanoclay as nucleation agents and to the development of plastic foaming technologies for plastic–nanoclay composites. However, this has yet to be achieved because cell nucleation and growth processes are often not observable in typical foaming equipment (e.g., extrusion foaming or injection foam molding). This study fills this gap through in situ observation of HDPE–nanoclay composites foaming blown with CO_2 using a foaming visualization system with a high-temperature/high-pressure view-cell (Wong et al. 2012).

Theoretical framework

Classical nucleation theory

According to the classical nucleation theory (CNT) (Gibbs 1961), a bubble that has a radius (R_{bub}) greater than the critical radius (R_{cr}) grows spontaneously, while one that has a radius smaller than R_{cr} collapses. The R_{cr} is state variable that depends on material, temperature, pressure, and concentration of blowing agent. A critical bubble (i.e., a bubble with radius equals to R_{cr}) is at an unstable equilibrium, where the free energy of the system (ΔF) is at a maximum (see Fig. 1). This maximum ΔF is called the free energy barrier for cell nucleation (W). Cell nucleation occurs when a bubble's radius (R_{bub}) grows beyond R_{cr}.

According to the CNT, cell nucleation occurs either within a continuous liquid phase (i.e., homogeneous nucleation), or on a liquid/liquid or liquid/solid interface (i.e., heterogeneous nucleation). By considering the change of ΔF from a state with no bubble to one where a bubble is generated homogeneous or heterogeneously, the equation of R_{cr} for both homogeneous and heterogeneous nucleation have been determined previously as (Gibbs 1961) (see "Appendix" section for details):

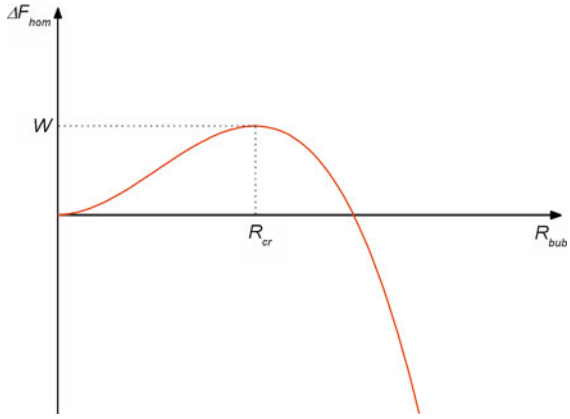

Fig. 1 ΔF versus R_{bub} plot

$$R_{cr} = \frac{2\gamma_{lg}}{P_{bub,cr} - P_{local}} \tag{1}$$

where γ_{lg} is the surface tension along the liquid–gas interface that constitutes the bubble, $P_{bub,cr}$ is the pressure inside a critical bubble, and P_{local} is the local pressure around the critical bubble. The free energy barrier for homogeneous nucleation (W_{hom}) and heterogeneous nucleation (W_{het}) has been determined previously as (Gibbs 1961):

$$W_{hom} = \frac{16\pi\gamma_{lg}^3}{3\left(P_{bub,cr} - P_{local}\right)^2} \tag{2}$$

$$W_{het} = \frac{16\pi\gamma_{lg}^3 F}{3\left(P_{bub,cr} - P_{local}\right)^2} = W_{hom}F \tag{3}$$

where F is the ratio of the volume of a heterogeneously nucleated bubble to that of a spherical bubble having the same radius of curvature (see "Cell nucleation from microvoids on nucleating agents" section for details). Since $F \leq 1$ in most scenarios, W_{het} is lower than W_{hom} in most cases. Therefore, nucleation is more likely to occur heterogeneously on nucleating agents or impurities as supposed to homogeneously within the bulk phase of a polymer–gas solution.

The concept of R_{cr}, W_{hom}, and W_{het} provides conditions to generate a metastable state necessary for cell nucleation. However, the CNT could not predict when a system would transfer, through molecular perturbation or external work, from a metastable liquid–gas solution to one where a bubble with size R_{cr} is generated within the liquid–gas solution; consideration of kinetics is necessary to determine the rate of cell nucleation, and hence cell density. In this context, Blander and Katz (1975) defined bubble nucleation rate, J, as the rate at which critical bubbles gain gas molecules that trigger their spontaneous growth to become nucleated bubbles. The expressions for J for homogeneous and heterogeneous nucleation, J_{hom} and J_{het}, have been derived previously as (Blander and Katz 1975):

$$J_{hom} = N\sqrt{\frac{2\gamma_{lg}}{\pi m}}\exp\left(-\frac{W_{hom}}{k_B T_{sys}}\right) \tag{4}$$

$$J_{het} = N^{\frac{2}{3}}Q\sqrt{\frac{2\gamma_{lg}}{\pi m F}}\exp\left(-\frac{W_{het}}{k_B T_{sys}}\right) \tag{5}$$

where N is the number of gas molecules per unit volume of polymer; Q is the ratio of the surface area of the heterogeneously nucleated bubble to that of a spherical bubble with the same radius of curvature; m is the mass of a gas molecule; and k_B is the Boltzmann's Constant. The expression for cell density, $N(t)$ at time, t is the integral of the total cell nucleation rate:

$$N(t) = \int_0^t \{J_{hom}(t') + A_{het}J_{het}(t')\}dt' \tag{6}$$

where A_{het} is the total surface area of heterogeneous nucleating sites per unit volume of a polymer–gas solution. CNT describes boiling or cavitation phenomena in many single component systems accurately when extreme care has been used to remove any existing gas bubbles in the liquid phase (e.g., boiling of water). However, in plastic foaming processes, it has been demonstrated by various researchers that CNT often overestimates the degree of supersaturation ($P_{bub,cr} - P_{local}$) that is needed to initiate cell nucleation; the observed cell nucleation rates were significantly higher than were predicted by CNT (Lubetkin 2003). One of the criticisms of CNT was its assumption of continuum mechanics that ultimately led to overestimation of surface energies of nano-sized bubbles, and hence the energy barrier for cell nucleation (Kim et al. 2011). Other researchers proposed that microvoids exist in polymer–gas solutions as free volumes between polymer chains, or gas pockets on solid particles (e.g., nucleating agents, impurities, etc.) due to the high viscosity of plastic melt and contact angle restraint (Harvey et al. 1944; Levy 1981; Ward and Levart 1984). The free energy required for cell

nucleation from the growth of existing microvoids would be lower than that predicted by CNT. Based on this concept, CNT and the corresponding kinetic theory for nucleation discussed above have been extended in this study to include cell nucleation from existing microvoids.

Cell nucleation from microvoids within bulk phase of polymer–gas solution

Given a scenario where a gas bubble exists within the bulk phase of a polymer/gas solution (see Fig. 2ii). The free energy change (ΔF_{hom}) from a bubble with volume of $V_{g,1}$ and surface area of $A_{g,1}$ (State 1) to a larger gas bubble with volume of $V_{g,2}$ and surface area of $A_{g,2}$ (State 2) within the polymer/gas solution could be given as:

$$\begin{aligned}\Delta F_{\text{hom}} = &-\left(P_{\text{bub},2}-P_{\text{local}}\right)V_{g,2}+\gamma_{lg}A_{lg,2}\\ &-\left[-\left(P_{\text{bub},1}-P_{\text{local}}\right)V_{g,1}+\gamma_{lg}A_{lg,1}\right]\end{aligned} \tag{7}$$

where and P_{bub} is the pressure inside the bubble. Assuming that the bubble is spherical, Eq. 7 could be simplified to:

$$\begin{aligned}\Delta F_{\text{hom}} = &-\frac{4\pi R_{\text{bub},2}^3}{3}\left(P_{\text{bub},2}-P_{\text{local}}\right)+\gamma_{lg}\left(4\pi R_{\text{bub},2}^2\right)\\ &-\left[-\frac{4\pi R_{\text{bub},1}^3}{3}\left(P_{\text{bub},1}-P_{\text{local}}\right)\right.\\ &\left.+\gamma_{lg}\left(4\pi R_{\text{bub},1}^2\right)\right]\end{aligned} \tag{8}$$

of R_{cr} to Eq. 8, the free energy barrier of cell nucleation from an existing microvoid (W_{hom}) within the bulk phase of a polymer–gas solution could be simplified to:

$$\begin{aligned}W_{\text{hom}} = &\frac{16\pi\gamma_{lg}^3}{3\left(P_{\text{bub,cr}}-P_{\text{local}}\right)^2}\\ &-\frac{4\pi R_{\text{bub},1}^2}{3}\left[\left(P_{\text{local}}-P_{\text{bub},1}\right)R_{\text{bub},1}+3\gamma_{lg}\right]\end{aligned} \tag{9}$$

The first term on the right hand side is the free energy barrier to nucleate a bubble homogeneously within a polymer–gas solution without the presence of an existing microvoid (same as Eq. 2). The second term on the right hand side is the free energy change from a metastable polymer–gas solution to the homogeneous formation of a gas bubble with a size of $R_{\text{bub},1}$ within the polymer–gas solution. As demonstrated by this equation, the overall W_{hom} is decreased when cell nucleation occurs through the growth of an existing microvoid. Therefore, if there are microvoids within a polymer–gas solution, cell nucleation is likely to occur via the growth of these microvoids as supposed to homogeneous nucleation within the bulk phase of the polymer–gas solution. Due to the presence of existing microvoids, the cell nucleation rate and hence the cell density are expected to increase. Based on the expression for the classical homogeneous cell nucleation rate (J_{het}) (Eq. 4) and Eq. 9, the cell nucleation rate from the growth of microvoids within a bulk phase of polymer–gas solution could be derived to be:

$$J_{\text{hom}} = \int_{R_{\text{bub},1}} \rho_R N\sqrt{\frac{2\gamma_{lg}}{\pi m}}\exp\left\{-\frac{1}{k_B T_{\text{sys}}}\left(\begin{array}{l}\frac{16\pi\gamma_{lg}^3}{3\left(P_{\text{bub,cr}}-P_{\text{local}}\right)^2}\\ -\frac{4\pi R_{\text{bub},1}^2}{3}\left[\left(P_{\text{local}}-P_{\text{bub},1}\right)R_{\text{bub},1}+3\gamma_{lg}\right]\end{array}\right)\right\}\mathrm{d}R_{\text{bub},1} \tag{10}$$

where R_{bub} is the bubble radius. Both $P_{\text{bub},1}$ and $R_{\text{bub},1}$ are independent of $R_{\text{bub},2}$. By taking the derivative of ΔF_{hom} with respect to $R_{\text{bub},2}$ and equating it to zero, the expression of R_{cr} could be shown to be the same as the CNT case (see Eq. 1). By substituting the expression

where $\rho_R(R_{\text{bub},1})$ is the probability density function of the size of existing microvoids ($R_{\text{bub},1}$). If no microvoid exists (i.e., homogeneous nucleation of CNT), then $\rho_R(R_{\text{bub},1}=0)=1$. In that case, Eq. 10 would be reduced to the original form (Eq. 4).

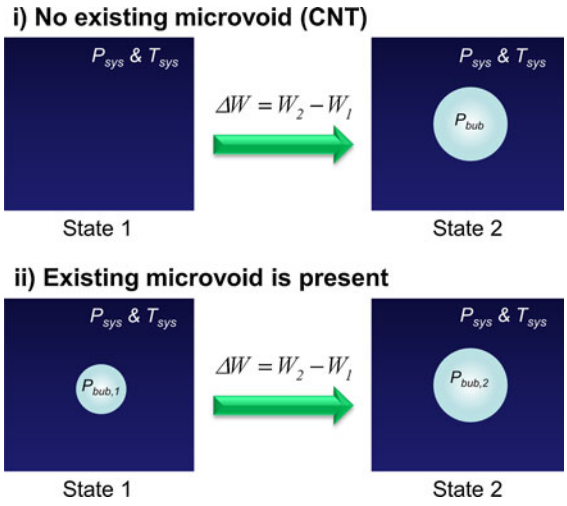

Fig. 2 Homogeneous nucleation of CNT versus nucleation through growth of a microvoid in polymer–gas solution

Cell nucleation from microvoids on nucleating agents

As mentioned earlier, nucleating agents (e.g., nanoclay, talc, etc.) are often added to polymer matrix to enhance bubble nucleation. These nucleating agents and/or their agglomerates (e.g., intercalated nanoclay particles) might have non-uniform surfaces that could be modelled as conical cavities (Cole 1974; Leung et al. 2006). This scenario is illustrated in Fig. 3. Based on this scenario, the free energy change (ΔF_{het}) from a microvoid with a radius of curvature of $R_{bub,1}$

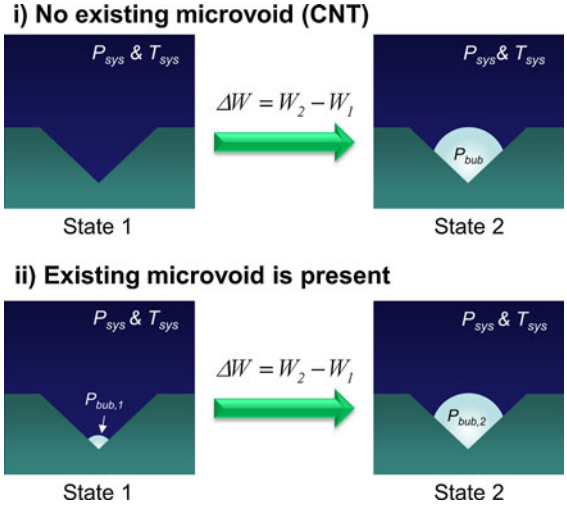

Fig. 3 Heterogeneous nucleation of CNT versus nucleation through growth of a microvoid on a conical cavity

on a nucleating site (State 1) to a larger microvoid with a radius of curvature of $R_{bub,2}$ on the same nucleating site (State 2) within a polymer–gas solution could be determined using a similar approach described above:

$$\begin{aligned}\Delta F_{het} = &-\left(P_{bub,2} - P_{local}\right)V_{g,2} + \left(\gamma_{sg} - \gamma_{sl}\right)A_{sg,2} \\ &+ \gamma_{lg}A_{lg,2} - \left[-\left(P_{bub,1} - P_{local}\right)V_{g,1}\right. \\ &\left.+\left(\gamma_{sg} - \gamma_{sl}\right)A_{sg,1} + \gamma_{lg}A_{lg,1}\right] \end{aligned} \quad (11)$$

where V_g is the volume of the bubble; A_{sg} and A_{lg} are the area of the solid–gas and liquid–gas interfaces, respectively; and γ_{sg}, γ_{sl}, and γ_{lg} are the surface tension along the solid–gas, solid–liquid, and liquid–gas interfaces, respectively. Using the Young's equation, which relates the interfacial energies and the contact angle (θ_c) between the liquid and gas phase (measured in the liquid phase) (Ward and Tucker 1975):

$$\gamma_{sg} - \gamma_{sl} = \gamma_{lg}\cos\theta_c \quad (12)$$

and the expressions for V_g, A_{sg}, and A_{lg} for a microvoid on a conical cavity (Cole 1974), Eq. 11 could be simplified to:

$$\begin{aligned}\Delta F_{het} = &-\frac{4\pi R_{bub,2}^3}{3}\left(P_{bub,2} - P_{local}\right)F + 4\pi R_{bub,2}^2\gamma_{lg}F \\ &-\left[-\frac{4\pi R_{bub,1}^3}{3}\left(P_{bub,1} - P_{local}\right)F + 4\pi R_{bub,1}^2\gamma_{lg}F\right]\end{aligned} \quad (13)$$

The expression for F describing a conical cavity has been derived to be (Cole 1974):

$$F(\theta_c,\beta) = \frac{1}{4}\left[2 - 2\sin(\theta_c - \beta) + \frac{\cos\theta_c\cos^2(\theta_c - \beta)}{\sin\beta}\right] \quad (14)$$

where β is the semi-conical angle of a conical cavity. Both $P_{bub,1}$ and $R_{bub,1}$ are independent of $R_{bub,2}$. By taking the derivative of ΔF_{het} with respect to $R_{bub,2}$ and equating it to zero, the expression of R_{cr} could be shown to be the same as the CNT case (see Eq. 1). By substituting R_{cr} to Eq. 13, the free energy barrier of cell nucleation from an existing microvoid on a conical cavity (W_{het}) could be determined to be:

$$\begin{aligned}W_{het} = &\frac{16\pi\gamma_{lg}^3 F}{3\left(P_{bub,cr} - P_{local}\right)^2} \\ &-\frac{4\pi R_{bub,1}^2 F}{3}\left[\left(P_{local} - P_{bub,1}\right)R_{bub,1} + 3\gamma_{lg}\right]\end{aligned} \quad (15)$$

The first term on the right hand side is the free energy barrier to nucleate a bubble heterogeneously on a conical cavity within a polymer–gas solution and without the presence of an existing microvoid (same as Eq. 3). The second term on the right hand side is the free energy change from a state with a conical cavity within a metastable polymer–gas solution to the formation of a gas bubble with a size of $R_{\text{bub},1}$ on the conical cavity within the polymer–gas solution. As shown in Eq. 15, the overall W_{het} is decreased if cell nucleation occurs through the growth of an existing microvoid on a conical cavity. Therefore, if there are microvoids on cavities (e.g., on nucleating agents, impurities, or equipment surfaces, etc.), cell nucleation are likely to occur through the growth of these microvoids as supposed to heterogeneous nucleation without the presence of microvoids. These microvoids are more likely to exist if there are poor interface between the polymer–gas mixture and the surfaces of nucleating agents. Moreover, in the presence of flow, tensile, and/or shear stresses might cause the polymer–gas mixture to be dewetted from the nucleating agent, thus generating more microvoids for cell nucleation. Therefore, due to the presence of these microvoids, the cell nucleation rate and hence the cell density are expected to increase. Based on the expression for classical heterogeneous cell nucleation rate (J_{het}) (Eq. 5), the heterogeneous cell nucleation rate from microvoids could be derived to be:

$$J_{\text{het}} = \int_{\beta}\int_{R_{\text{bub},1}} \rho_{\beta}\rho_{R}N_{\frac{2}{3}}^{2}Q\sqrt{\frac{2\gamma_{\text{lg}}}{\pi m F}}\exp\left\{-\frac{1}{k_{\text{B}}T_{\text{sys}}}\left(\begin{array}{l}\frac{16\pi\gamma_{\text{lg}}^{3}F}{3\left(P_{\text{bub,cr}}-P_{\text{local}}\right)^{2}} \\ -\frac{4\pi R_{\text{bub},1}^{2}F}{3}\left[\left(P_{\text{local}}-P_{\text{bub},1}\right)R_{\text{bub},1}+3\gamma_{\text{lg}}\right]\end{array}\right)\right\}\mathrm{d}R_{\text{bub},1}\mathrm{d}\beta \qquad (16)$$

where $\rho_{\beta}(\beta)$ is the probability density function of the semi-conical angle (β) of conical cavities and $\rho_{R}(R_{\text{bub},1})$ is the probability density function of the size of existing microvoids ($R_{\text{bub},1}$). Note that the value of β could also influence the distribution of $R_{\text{bub},1}$. If no microvoid exists (i.e., the case for the classical heterogeneous nucleation), then $\rho_{R}(R_{\text{bub},1} = 0) = 1$. In that case, Eq. 16 would be reduced to the original form (Eq. 5).

Experimental materials and procedure

The HDPE–nanoclay composites were prepared using melt compounding with an extrusion system (Lee et al. 2007a). The materials forming the composites were: HDPE (Sclair 2607, Nova Chemicals, MFI = 5.0 g/10 min), HDPE-g-maleic anhydride (PE-g-MAn, Fusabond MB-100D, Dupont, MFI = 0.96 g/10 min), and organoclay (Cloisite 20A, Southern Clay Products). The PE-g-MAn served as a compatibilizer to achieve exfoliation of nanoclay. The intercalated HDPE-nanocomposite was prepared by mixing HDPE with 0.5 wt% nanoclay (labeled as HNC0.5). The exfoliated sample was prepared by compounding HDPE (49.5 wt%), PE-g-MAn (50 wt%), and nanoclay (0.5 wt%) and was labeled as HWC0.5. Neat HDPE and a mixture of HDPE (50 wt%) and PE-g-MAn mixture (50 wt%) were also studied (labeled as HNC0 and HWC0, respectively). By wide-angle X-ray diffraction (XRD) measurements, Lee et al. (2007a) demonstrated that the HWC0.5 has a significantly improved degree of exfoliation of nanoclay over HNC0.5. To be specific, the diffraction peak that characterized the interlayer spacing of stacks of nanoclay platelets was not found in the HWC0.5 sample, and the corresponding TEM image showed that delaminated nanoclay platelets were uniformly distributed in the sample (see Fig. 4). Therefore, it was considered as the exfoliated sample in this study. On the other hand, the diffraction peak that characterized the interlayer spacing of stacks of nanoclay platelets was found in the HNC0.5 sample, and the nanoclay particles were significantly larger and thicker, as shown in the corresponding TEM image. This demonstrated that the HNC0.5 sample was not exfoliated. The angle of diffraction peak was smaller than that of nanoclay, which indicated that the interlayer spacing increased as a result of the extrusion compounding

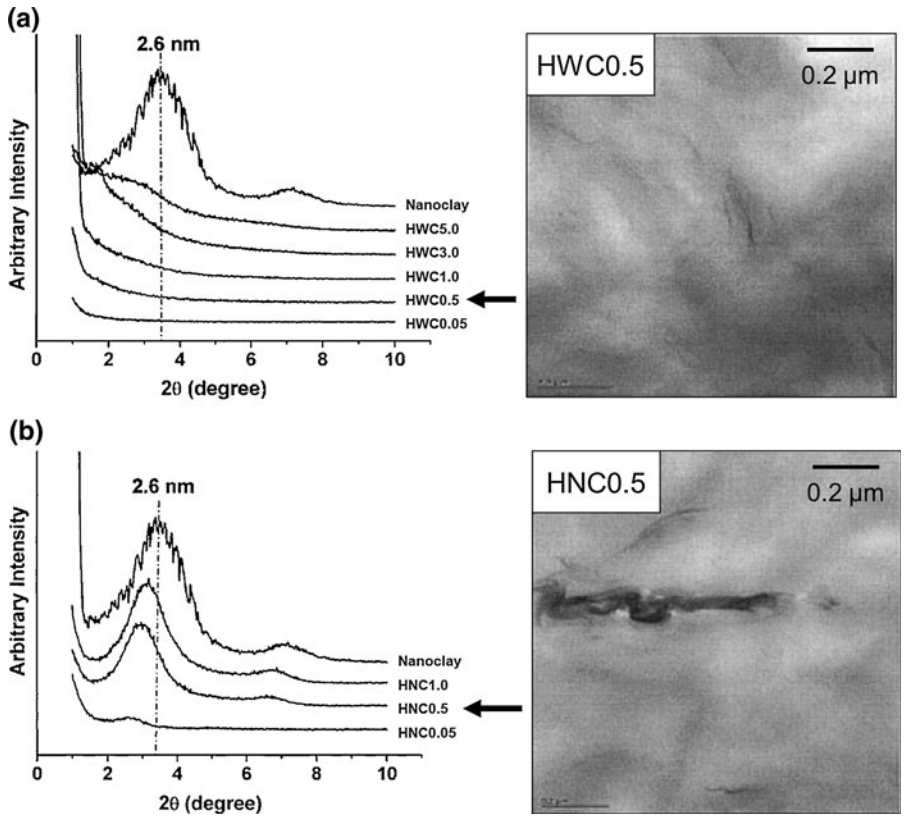

Fig. 4 XRD diffraction patterns and TEM of **a** HWC composites; **b** HNC composites (Lee et al. 2007a)

process. Therefore, it was considered as the intercalated sample in this study.

By comparing the foaming behavior of the HNC and HWC composites, the exfoliation effect on foaming were elucidated. Experiments were conducted with a foaming visualization with a high-temperature/high-pressure view-cell (see Fig. 5) to capture the foaming processes under high-speed and micro-scale (Wong et al. 2012). To conduct an experiment, a thin HDPE film (6.3 mm in diameter and 0.4 mm in thickness) was placed inside the view-cell to allow dissolution of CO_2 at high-temperature and pressure for 30 min. The plastic sample was placed on top of a thin PET film with a 1-mm hole at the center; observation and characterization was made at the suspended region to eliminate the heterogeneous nucleating effect of the PET films and the sapphire lens underneath. Foaming was induced by a rapid depressurization and was captured with a high-speed camera. Three saturation pressures (P_{sat}) were used: 6 MPa (870 psi), 7.6 MPa (1100 psi), and 10.3 MPa (1500 psi). Meanwhile, the foaming temperature (T_{sys}) was kept at 180 °C for all cases. The T_{sys} was chosen at a high temperature to ensure that polymer is in the melt state, thus eliminating any effect of crystals on cell nucleation and growth. Each experimental case was conducted three times. For analysis, cell density data was extracted from the foaming visualization data. To achieve this, $N(t)$, the number of cells within a superimposed circular boundary with an area of A_c at time t, was counted at each time frame. The radii of 10 randomly selected bubbles at each time frame (i.e., $R_{bub,i}(t)$, where $i = 1 \ldots 10$) were also measured. The cell density with respect to the foamed volume, $N_{foam}(t)$, and the cell density with respect to the unfoamed volume, $N_{unfoam}(t)$, were calculated using the following equations:

$$N_{foam}(t) = \left(\frac{N(t)}{A_c}\right)^{\frac{3}{2}} \tag{17}$$

$$N_{unfoam}(t) = N_{foam}(t) \times \mathrm{VER}(t) \tag{18}$$

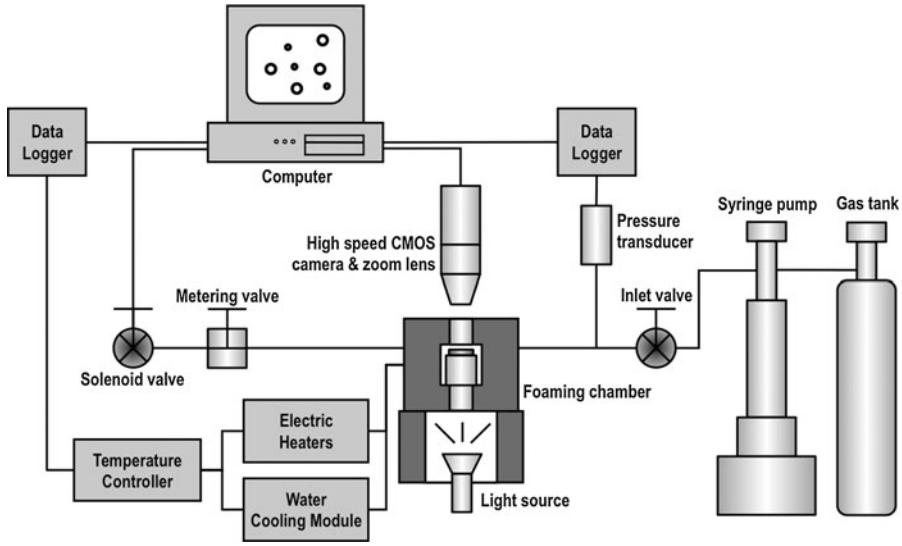

Fig. 5 Foaming visualization system with a high-temperature/high-pressure view-cell (Wong et al. 2012)

$$\mathrm{VER}(t) = 1 + \left(\frac{4}{3}\pi\left(\sum_{i}^{10}\frac{R_{\mathrm{bub},i}(t)^3}{10}\right) \times N_{\mathrm{foam}}(t)\right) \tag{19}$$

where VER(t) is the volume expansion ratio of the foam at time t. The data was collected from $t = 0$ to after the completion of cell nucleation process to extract the cell density versus time data. Note that the smallest cells that could be observed were approximately 2–5 μm in diameter (Wong et al. 2007). Therefore, there could be a small time delay between cell nucleation and the instant at which cells were observed. Therefore, the cell density profiles were based on the observable cells only. Also, a line-of-best-fit was generated for the cell radius versus time data of each measured cell (30 cells for each experimental case). Subsequently, the average bubble growth rate of each case was obtained by taking the average of the slopes of the lines-of-best-fit.

Results and discussion

Snapshots of the foaming visualization data for $P_{\mathrm{sat}} = 6.0$ MPa (870 psi), 7.6 MPa (1100 psi), and 10.3 MPa (1500 psi) are shown in Fig. 6a–c, respectively. For the $P_{\mathrm{sat}} = 6.0$ and 7.6 MPa cases, no cell was nucleated in the suspended region of the samples with no nanoclay added (HNC0 and HWC0). Meanwhile, cells were nucleated in the surrounding regions, where the samples were in contact with the PET surface because the PET surfaces act as heterogeneous nucleation sites, which decreased the energy barrier for nucleation. This demonstrated that the heterogeneous nucleation effect of the PET surface was significant, and observation had to be made in the suspended region in order to study the effect of nanoclay in an isolated manner. For the samples with nanoclay (HNC0.5 and HWC0.5) at these pressures, cell nucleation occurred in the suspended region for the HNC0.5 sample (with intercalated nanoclay), but not for the HWC0.5 sample (with exfoliated nanoclay). For the $P_{\mathrm{sat}} = 10.3$ MPa cases (see Fig. 6c), all four samples were foamed in the suspended region due to the increased gas concentration that led to higher supersaturation level and lower γ_{lg} that resulted in lower W_{hom} and W_{het}. As shown in Fig. 7a, b, the maximum cell density of the HNC0.5 and HWC0.5 cases ($N_{\mathrm{unfoam}} = 3.2 \times 10^6$ and 2.6×10^6 cells/cm^3, respectively) were higher than the HNC0 and HWC0 cases ($N_{\mathrm{unfoam}} = 5.2 \times 10^5$ and 9.1×10^5 cells/cm^3, respectively), which demonstrated the nucleating power of nanoclay. The HWC0 sample resulted in slightly higher maximum cell density than the HNC0 sample. On the other hand, the maximum cell density of the HNC0.5 case was higher than the HWC0.5 case. Figure 7c summarized the cell density data for all experimental cases; it demonstrated that the HNC0.5 samples resulted in the highest cell densities at all three P_{sat}. This result might seem counter-intuitive because it is commonly believed that the particle density and interfacial area for heterogeneous

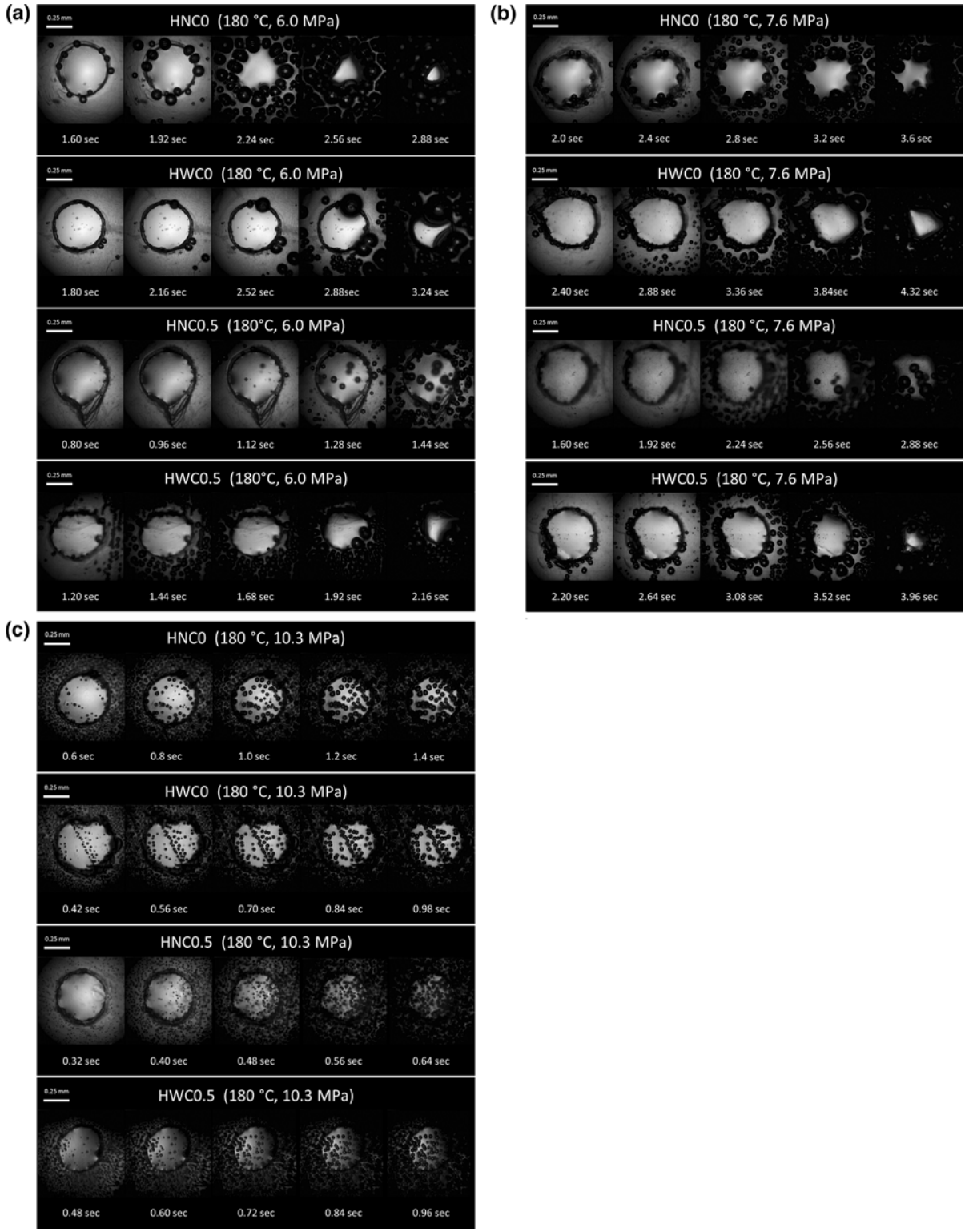

Fig. 6 Snapshots of in situ foaming visualization data: **a** $P_{sat} = 6.0$ MPa; **b** $P_{sat} = 7.6$ MPa; **c** $P_{sat} = 10.3$ MPa

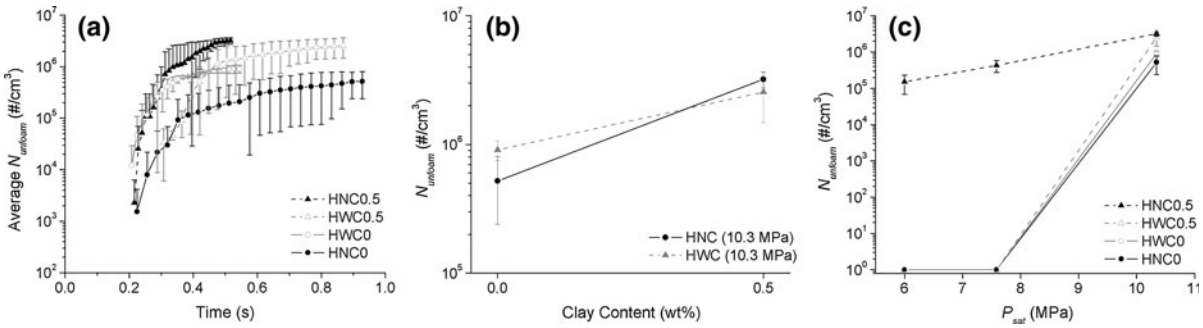

Fig. 7 Cell density data: **a** N_{unfoam} versus time ($P_{sat} = 10.3$ MPa); **b** maximum cell density ($P_{sat} = 10.3$ MPa); **c** maximum cell density (all cases). (Note: 10^0 signify zero cell density)

nucleation should be significantly higher in the sample with exfoliated nanoclay (HWC0.5). This should have led to a higher cell density, according to Eq. 6.

There are two main reasons for the superior cell nucleating performance of the intercalated nanoclay over the exfoliated one. The first reason is the stress-induced nucleation effect. As cells nucleated and grew near a nanoclay particle, the local pressure (P_{local}) around the particle might not equal to the system pressure (P_{sys}) as the flow field of the polymer–gas solution would be changed by the presence of the nanoclay particle. Consequently, the polymer–gas solution could be subjected to local pressure variations (ΔP_{local}) in these regions. Wang et al. (2010) demonstrated this behavior by conducting a numerical simulation of the pressure field of a polymer–gas solution around a solid particle near the presence of a growing bubble; it was found that tensile stresses could exist in some regions around the particle. Due to the tensile stresses, the local system pressure would be lowered, which increased the supersaturation level in those regions. Consequently, cell nucleation would likely occur in these regions. This stress-induced nucleation theory was first proposed by Albalak et al. (1990), and was later confirmed by Leung et al. (2012) and Wong et al. (2011) via foaming visualization studies of PS–talc composites. To account for these local pressure variations (ΔP_{local}), the expression for R_{cr} (Eq. 1) has been previously modified as follows (Leung et al. 2012; Wong et al. 2011):

$$R_{cr} = \frac{2\gamma_{lg}}{P_{bub,cr} - \left(P_{sys} + \Delta P_{local}\right)} \tag{20}$$

When there is a tensile stress, ΔP_{local} would be negative, hence the P_{local} would decrease and the supersaturation level would increase. Similarly, the expression of W_{hom} (Eq. 9), J_{hom} (Eq. 10), W_{het} (Eq. 15), and J_{het} (Eq. 16) could be modified, respectively, to be:

$$W_{hom} = \frac{16\pi\gamma_{lg}^3}{3\left(P_{bub,cr} - \left(P_{sys} + \Delta P_{local}\right)\right)^2} - \frac{4\pi R_{bub,1}^2}{3}\left[\left(\left(P_{sys} + \Delta P_{local}\right) - P_{bub,1}\right)R_{bub,1} + 3\gamma_{lg}\right] \tag{21}$$

$$J_{hom} = \int_{R_{bub,1}} \rho_R N \sqrt{\frac{2\gamma_{lg}}{\pi m}} \exp\left\{-\frac{1}{k_B T_{sys}}\left(\begin{array}{l}\frac{16\pi\gamma_{lg}^3}{3\left(P_{bub,cr} - \left(P_{sys} + \Delta P_{local}\right)\right)^2} \\ -\frac{4\pi R_{bub,1}^2}{3}\left[\left(\left(P_{sys} + \Delta P_{local}\right) - P_{bub,1}\right)R_{bub,1} + 3\gamma_{lg}\right]\end{array}\right)\right\} dR_{bub,1} \tag{22}$$

$$W_{het} = \frac{16\pi\gamma_{lg}^3 F}{3\left(P_{bub,cr} - \left(P_{sys} + \Delta P_{local}\right)\right)^2} - \frac{4\pi R_{bub,1}^2 F}{3}\left[\left(\left(P_{sys} + \Delta P_{local}\right) - P_{bub,1}\right)R_{bub,1} + 3\gamma_{lg}\right] \tag{23}$$

$$J_{\text{het}} = \int_{\beta} \int_{R_{\text{bub},1}} \rho_{\beta}\rho_{R} N_{\frac{2}{3}}^{\frac{2}{3}} Q \sqrt{\frac{2\gamma_{\text{lg}}}{\pi m F}} \exp\left\{ -\frac{1}{k_{\text{B}} T_{\text{sys}}} \left(\begin{array}{l} \frac{16\pi\gamma_{\text{lg}}^{3} F}{3\left(P_{\text{bub,cr}} - \left(P_{\text{sys}} + \Delta P_{\text{local}}\right)\right)^{2}} \\ -\frac{4\pi R_{\text{bub},1}^{2} F}{3}\left[\left(\left(P_{\text{sys}} + \Delta P_{\text{local}}\right) - P_{\text{bub},1}\right) R_{\text{bub},1} + 3\gamma_{\text{lg}}\right] \end{array} \right) \right\} \mathrm{d}R_{\text{bub},1}\mathrm{d}\beta \tag{24}$$

The intercalated nanoclay particles had larger particle sizes than the exfoliated ones (see Fig. 4), and were also expected to be stiffer due to their multilayer structures. Because of this, the intercalated nanoclay particles would be more restricted to move with the flow of the polymer–gas solution as cells grew around its vicinity. This would result in higher tensile stresses (e.g., negative ΔP_{local}) in localized regions around the particles, which decreased the energy barrier for nucleation, and hence the cell nucleation rate would be increased (see Eq. 24). This result is similar to the PS foaming visualization study by Wong and Park (2012), where talc with different sizes were used as nucleating agents to investigate the effect of talc sizes on cell nucleating performance. In that study, it was observed that the type of talc with the largest sizes resulted in the highest cell density despite its lowest particle density when the same weight content of talc was used. Similar to this study, it was believed that the primary reason for this behavior was the stress-induced cell nucleation phenomena. Because of this foaming mechanism, intercalated nanoclay was more effective in generating cells despite its lower particle density and interfacial area for heterogeneous nucleation. On the other hand, Lee et al. (2007a) showed that HWC0.5 possessed higher viscosity and elasticity than HNC0.5 due to the well-dispersed exfoliated nanoclay and the PE-g-MAn. In theory, this could lead to higher level of tensile stresses in presence of nearby growing bubbles, and hence stress-induced nucleation could be enhanced. However, the particle size and stiffness effects on stress-induced nucleation seemed to be more dominant at the experimental conditions used in this study.

Another reason for the better cell nucleating performance of the intercalated nanoclay was its lower polymer–nanoclay surface affinity when compared to the exfoliated one. As mentioned earlier, PE-g-MAn has been used for the HWC0.5 sample (exfoliated case) to improve the distribution and exfoliation of nanoclay in the HDPE matrix. The PE-g-MAn would increase the affinity between the nanoclay surface and the HDPE matrix. This would decrease the contact angle (θ_{c}) as the polymer tended to wet on the surface of the nanoclay. Consequently, the geometric factor F (i.e., the ratio of the volume of a nucleated bubble to the volume of a spherical bubble with the same radius of curvature) would increase. To illustrate this, a 3D plot of F as a function of θ_{c} and β has been generated using Eq. 14 (see Fig. 8). This figure demonstrates that F increased significantly as θ_{c} decreased. It is believed this is an important reason behind the decreased nucleating power of the exfoliated nanoclay in the HDPE nanocomposites because cell nucleation rate and cell density is highly sensitive to changes in θ_{c}. For example, a numerical simulation of PS foaming with CO_2 demonstrated that the cell density increased by four orders of magnitude (i.e., from 10^5 to 10^9 cells/cm^3) due to a small change of θ_{c} from 85.5° to 87.5° (Leung et al. 2006). Also, with an increase of the polymer–nanoclay surface affinity, the polymer–gas solution would be more likely to wet on

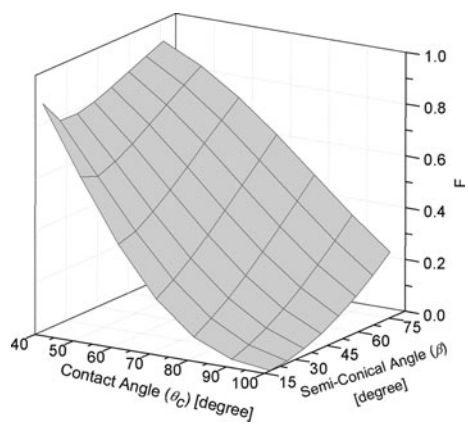

Fig. 8 F versus θ_{c} and β plot

any nano- or micro-sized crack or cavities on the nanoclay particles; thus, it would less likely for microvoids to exist under high-temperatures and pressures. Therefore, nucleation from microvoids, which was thermodynamically favorable, would be less dominant in the HWC0.5 case. Meanwhile, intercalated nanoclay particles would have irregular surfaces due to their multi-layer structure of clay platelets. Gas clusters could be trapped on surfaces or between layers of clay platelets to act as seeds for nucleation. This further explained the inferior nucleation performance of the exfoliated nanoclay when compared to the intercalated ones.

The average cell growth rates for all four samples (HNC0, HWC0, HNC0.5, and HWC0.5) were characterized based on the method described in "Experimental materials and procedure" section. Comparison between all samples was made at $P_{sat} = 10.3$ MPa (1500 psi) only because that was the only experimental condition at which all samples were foamed (see Fig. 9). Compared to HNC0, the HWC0 seemed to have slightly lower cell growth rate, which could be attributed to the higher viscosity of the HWC0 sample due to the addition of PE-g-MAn. However, the differences were not statistically significant due to the large variations of the cell growth rate data. Also, the addition of intercalated nanoclay did not seem to hinder cell growth (see HNC0.5 in Fig. 9) as the average cell-growth rate remained at a similar level. On the other hand, the exfoliated nanoclay seemed to have effectively hindered the average cell-growth rates (see HWC0.5 in Fig. 9).

Moreover, during bubble growth, nanoclay particles tended to align to cell boundary due to biaxial extensional flow of polymer–gas solution (see Fig. 10). This has previously been demonstrated by Okamoto et al. (2001) via TEM imaging of foamed PP–nanoclay composites. The alignment of nanoclay particles increased the melt strength of the polymer nanocomposites along cell walls, which prevented cell wall rupture, and hence cell coalescence. Exfoliated nanoclay had a higher particle number and better polymer interaction than the intercalated counterpart; hence, the melt strength improvement of the exfoliated nanoclay case was expected to be higher than the intercalated case. Also, the alignment of nanoclay particles generated tortuous structures that would act as a barrier to hinder gas diffusion. This would effectively prevent cell coarsening (i.e., the collapse of

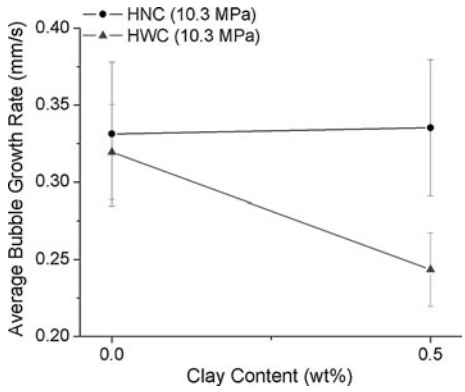

Fig. 9 Average bubble growth rate ($P_{sat} = 10.3$ MPa). (Note: *error bars* signify one standard deviation among 30 sets of cell radius data)

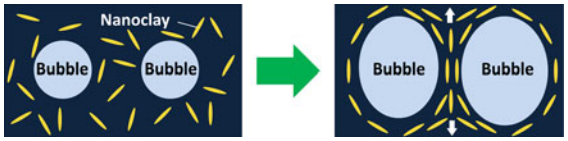

Fig. 10 Alignment of nanoclay particles during bubble growth

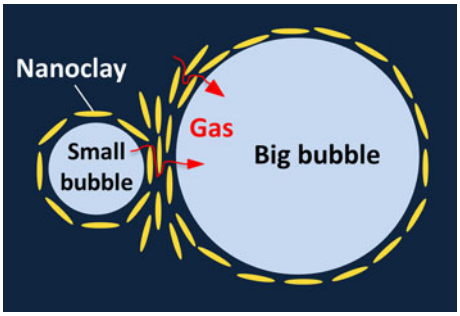

Fig. 11 Aligned nanoclay particles act as gas diffusion barrier

small cells adjacent to larger ones due to gas diffusion from the small cells to the large cells) (see Fig. 11). This behavior was believed to be more significant for the exfoliated nanoclay case due to its higher particle density.

Due to the superior cell stabilization characteristics of the exfoliated nanoclay, the cellular morphology of HDPE foams with exfoliated nanoclay might be better (e.g., cells with uniform cell sizes, closed-cell morphology, etc.) than those with intercalated nanoclay, despite of their inferior cell nucleating characteristics. However, due to the high processing temperature used

and the difficulty to instantly cool the foam sample to stabilize the cellular structure, cell deterioration was unavoidable in this study. Therefore, the stabilized foam samples could not be used to further investigate the effect of exfoliation of nanoclay on the cell stabilization characteristics and the final cell structure. Nevertheless, the cell growth rate data provided evidences of the superior cell stabilization characteristics of the exfoliated nanoclay.

Conclusion

Through in situ foaming visualization via a high-temperature/high-pressure view-cell system, the cell nucleation and growth behaviors of HDPE–nanoclay composites have been examined to elucidate the effects of intercalation and exfoliation of nanoclay. Intercalated nanoclay was found to be more effective in inducing cell nucleation, despite its lower particle density and smaller interfacial area for heterogeneous nucleation. This was caused by stress-induced cell nucleation, lower polymer–nanoclay affinity and higher number of existing gas cavities for cell nucleation. On the other hand, the cell stabilization capability of exfoliated nanoclay was superior to the intercalated nanoclay. This could be attributed to its higher melt strength and gas barrier properties, which would suppress cell coalescence and coarsening during cell stabilization.

Acknowledgments The authors of this paper are grateful to the Consortium of Cellular and Micro-Cellular Plastics (CCMCP) and Natural Sciences and Engineering Council of Canada (NSERC) for their financial support of this study.

Appendix: classical nucleation theory

The CNT and the concept of R_{cr} was first developed by Gibbs (1961). Over the years, various researchers have built on this theory to examine the necessary conditions and free energy barrier for homogeneous nucleation (Blander and Katz 1975; Ward et al. 1970; Forest and Ward 1976, 1978; Tucker and Ward 1975; Katz and Blander 1973) as well as heterogeneous nucleation with different surface geometries (Ward et al. 1983; Ward and Levart 1984; Cole 1974; Wilt 1986; Fisher 1948; Fletcher 1958; Apfel 1971; Jarvis et al. 1975).

Homogeneous nucleation

According to the CNT, the free energy change (ΔF_{hom}) from a metastable liquid–gas solution to the homogeneous formation of a gas bubble within the liquid can be given as (Tucker and Ward 1975; Ward et al. 1970):

$$\Delta F_{hom} = -(P_{bub} - P_{local})V_g + \gamma_{lg}A_{lg} \quad \text{(A1)}$$

where P_{bub} is the pressure inside the bubble; P_{local} is the system pressure surrounding the bubble; V_g is the bubble volume; γ_{lg} is the surface tension of the bubble–liquid interface; and A_{lg} is the bubble surface area. The first term on the left hand side (i.e., $-(P_{bub} - P_{local})V_g$) is the work done by the expansion of gas volume inside the bubble, and the second term (i.e., $\gamma_{lg}A_{lg}$) is the work required to create the liquid–gas interface that constitutes the bubble. Assuming that the bubble is spherical in shape, Eq. A1 can be rearranged as:

$$\Delta F_{hom} = -\frac{4\pi R_{bub}^3}{3}(P_{bub} - P_{local}) + \gamma_{lg}\left(4\pi R_{bub}^2\right) \quad \text{(A2)}$$

where R_{bub} is the radius of the bubble. Based on Eq. A2, a ΔF_{hom} versus R_{bub} plot can be generated (see Fig. 1), which exhibits a maximum ΔF_{hom} value. The maximum ΔF_{hom} represents the free energy barrier for homogeneous nucleation (W_{hom}), and the R_{bub} at which ΔF_{hom} is at the maximum is the R_{cr}. Since a system tends to seek a low energy configuration, a bubble smaller than R_{cr} tends to collapse, and a bubble larger than R_{cr} tends to grow spontaneously. By taking the derivative of ΔF_{hom} with respect to R_{bub} and equating it to zero, the R_{cr} could be determined as (Tucker and Ward 1975; Ward et al. 1970):

$$R_{cr} = \frac{2\gamma_{lg}}{P_{bub,cr} - P_{local}} \quad \text{(A3)}$$

where $P_{bub,cr}$ is the pressure inside a critical bubble. By substituting Eq. A3 into A2, the free energy barrier for homogeneous nucleation (W_{hom}) can be determined to be (Tucker and Ward 1975; Ward et al. 1970):

$$W_{hom} = \frac{16\pi\gamma_{lg}^3}{3\left(P_{bub,cr} - P_{local}\right)^2} \quad \text{(A4)}$$

Equation A4 indicates that W_{hom} is strongly dependent on γ_{lg} and the degree of supersaturation, which is

defined to be ($P_{bub,cr} - P_{local}$). A lower γ_{lg} and a higher degree of supersaturation would cause R_{cr} and W_{hom} to decrease, which lead to a higher tendency for bubble nucleation.

Heterogeneous nucleation

The derivation of R_{cr} and the free energy barrier for heterogeneous nucleation (W_{het}) could be formulated in a similar fashion. To be specific, the free energy change (ΔF_{het}) from a metastable liquid–gas solution to the heterogeneous formation of a gas bubble within the liquid on a liquid/solid interface can be given as (Ward et al. 1983; Ward and Levart 1984; Cole 1974; Wilt 1986; Fisher 1948; Fletcher 1958; Apfel 1971; Jarvis et al. 1975):

$$\Delta F_{het} = -(P_{bub} - P_{local})V_g + (\gamma_{sg} - \gamma_{sl})A_{sg} + \gamma_{lg}A_{lg} \quad (A5)$$

where γ_{sg} and γ_{sl} are the surface tension along the solid–gas interface and solid–liquid interface; and A_{sg} and A_{lg} is the surface area along the solid–gas and liquid–gas interface. Similar to the case of homogeneous nucleation, the first term on the left hand side (i.e., $-(P_{bub} - P_{local})V_g$) is the work done by the expansion of gas volume inside the bubble. The second term is the energy required to replace the solid–liquid interface (e.g., nucleating agent–polymer interface) with a solid–gas interface (e.g., nucleating agent–bubble interface). The third term (i.e., $\gamma_{lg}A_{lg}$) is the work required to create the liquid–gas interface that constitutes the bubble. Using the Young's equation, which relates the interfacial energies and the contact angle (θ_c) between the liquid and gas phase (measured in the liquid phase) (Ward and Tucker 1975):

$$\gamma_{sg} - \gamma_{sl} = \gamma_{lg}\cos\theta_c \quad (A6)$$

and the expressions for V_g, A_{sg}, and A_{lg} (which is specific to the surface geometry of the nucleating site), Eq. 11 can be simplified to:

$$\Delta F_{het} = -\frac{4\pi R_{bub}^3}{3}(P_{bub} - P_{local})F + 4\pi R_{bub}^2\gamma_{lg}F \quad (A7)$$

where F is a geometric factor that equals to the ratio of the volume of a heterogeneously nucleated bubble to that of a spherical bubble having the same radius of curvature. By taking the derivative of ΔF_{het} with respect to R_{bub} and equating the resulting equation to zero, it can be shown that the expression for R_{cr} is the same as the homogeneous nucleation case (Eq. A3). The expression for W_{het} can then be determined by substituting Eq. A3 into A7; which, after simplification, differs slightly from W_{hom}, as follows (Fisher 1948):

$$W_{het} = \frac{16\pi\gamma_{lg}^3 F}{3(P_{bub,cr} - P_{local})^2} = W_{hom}F \quad (A8)$$

Since $F \leq 1$ in most scenarios, W_{het} is lower than W_{hom} in most cases. Therefore, nucleation is more likely to occur heterogeneously on nucleating agents or impurities as supposed to homogeneously within the bulk phase of a polymer–gas solution.

References

Albalak RJ, Tadmor Z, Talmon Y (1990) Polymer melt devolatilization mechanisms. AlChE J 36(9):1313–1320

Apfel RE (1971) Vapor nucleation at a liquid–liquid interface. J Chem Phys 54:62–63

Blander M, Katz JL (1975) Bubble nucleation in liquids. AlChE J 21(5):833–848

Cole R (1974) Boiling nucleation. Adv Heat Transfer 10:85–166

Colton JS, Suh NP (1987a) Nucleation of microcellular thermoplastic foam with additives: part I: theoretical considerations. Polym Eng Sci 27(7):485–492

Colton JS, Suh NP (1987b) Nucleation of microcellular thermoplastic foam with additives: part II: experimental results and discussion. Polym Eng Sci 27(7):493–499

Fisher JC (1948) The fracture of liquids. J Appl Phys 19(11):1062–1067

Fletcher NH (1958) Size effect in heterogeneous nucleation. J Chem Phys 29(3):572–576

Forest TW, Ward CA (1976) Effect of a dissolved gas on the homogeneous nucleation pressure of a liquid. J Chem Phys 66(6):2322–2330

Forest TW, Ward CA (1978) Homogeneous nucleation of bubbles in solutions at pressures above the vapor pressure of the pure liquid. J Chem Phys 69(5):2221–2230

Giannelis EP (1996) Polymer layered silicate nanocomposites. Adv Mater 8(1):29–35

Gibbs JW (1961) The Scientific Papers of J. Willard Gibbs, vol 1. Dover Publications Inc., New York

Harvey EN, Barnes DK, McElroy WD, Whiteley AH, Pease DC, Cooper KW (1944) Bubble formation in animals. I. Physical factors. J Cell Comp Physiol 24(1):1–22

Jarvis TJ, Donohue MD, Katz JL (1975) Bubble nucleation mechanisms of liquid droplets superheated in other liquids. J Colloid Interface Sci 50(2):359–368

Katz JL, Blander M (1973) Condensation and boiling: corrections to homogeneous nucleation theory for nonideal gases. J Colloid Interface Sci 42(3):496–502

Kim Y, Park CB, Chen P, Thompson RB (2011) Origins of the failure of classical nucleation theory for nanocellular polymer foams. Soft Matter 7(16):7351–7358

Lee YH, Park CB, Sain M, Kontopoulou M, Zheng W (2007a) Effects of clay dispersion and content on the rheological, mechanical properties, and flame retardance of HDPE/clay nanocomposites. J Appl Polym Sci 105(4):1993–1999

Lee YH, Wang KH, Park CB, Sain M (2007b) Effects of clay dispersion on the foam morphology of LDPE/clay nanocomposites. J Appl Polym Sci 103(4):2129–2134

Leung SN, Park CB, Li H (2006) Numerical simulation of polymeric foaming processes using modified nucleation theory. Plast Rubber Compos Macromol Eng 35(3):93–100

Leung SN, Wong A, Wang C, Park CB (2012) Mechanism of extensional stress-induced cell formation in polymeric foaming processes with the presence of nucleating agents. J Supercrit Fluids 63:187–198

Levy S (1981) Advances in plastics technology. Van Nostrand Reinhold, New York

Lubetkin SD (2003) Why is it much easier to nucleate gas bubbles than theory predicts. Langmuir 19(7):2575–2587

Matuana LM, Park CB, Balatinecz JJ (1997) Processing and cell morphology relationships for microcellular foamed PVC/wood-fiber composites. Polym Eng Sci 37(7):1137–1147

Okamoto M, Nam PH, Maiti P, Kotaka T, Nakayama T, Takada M, Ohshima M, Usuki A, Hasegawa N, Okamoto H (2001) Biaxial flow-induced alignment of silicate layers in polypropylene/clay nanocomposite foam. Nano Lett 1(9):503–505

Seeler KA, Kumar V (1993) Tension–tension fatigue of microcellular polycarbonate: initial results. J Reinf Plast Compos 12(3):359–376

Shimbo M, Baldwin DF, Suh NP (1992) Viscoelastic behavior of microcellular plastics. In: American Chemical Society Division of Polymeric Materials—Science and Engineering, vol 67. ACS, Washington, DC, pp 512–513

Shimbo M, Higashitani I, Miyano Y (2007) Mechanism of strength improvement of foamed plastics having fine cell. J Cell Plast 43(2):157–167

Suh KW, Park CP, Maurer MJ, Tusim MH, De Genova R, Broos R, Sophiea DP (2000) Lightweight cellular plastics. Adv Mater 12(23):1779–1789

Taki K, Yanagimoto T, Funami E, Okamoto M, Ohshima M (2004) Visual observation of CO_2 foaming of polypropylene-clay nanocomposites. Polym Eng Sci 44(6):1004–1011

Tanoue S, Utracki LA, Garcia-Rejon A, Tatibouët J, Cole KC, Kamal MR (2004) Melt compounding of different grades of polystyrene with organoclay. Part 1: compounding and characterization. Polym Eng Sci 44(6):1046–1060

Ton-That MT, Perrin-Sarazin F, Cole KC, Bureau MN, Denault J (2004) Polyolefin nanocomposites: formulation and development. Polym Eng Sci 44(7):1212–1219

Tucker AS, Ward CA (1975) Critical state of bubbles in liquid–gas solutions. J Appl Phys 46(11):4801–4808

Usuki A, Kojima Y, Kawasumi M, Okada A, Fukushima Y, Kurauchi T, Kamigaito O (1993) Synthesis of nylon 6-clay hybrid. J Mater Res 8(5):1179–1184

Wang C, Leung SN, Bussmann M, Zhai WT, Park CB (2010) Numerical investigation of nucleating-agent-enhanced heterogeneous nucleation. Ind Eng Chem Res 49(24):12783–12792

Ward CA, Levart E (1984) Conditions for stability of bubble nuclei in solid surfaces contacting a liquid–gas solution. J Appl Phys 56(2):491–500

Ward CA, Tucker AS (1975) Thermodynamic theory of diffusion-controlled bubble growth or dissolution and experimental examination of the predictions. J Appl Phys 46(1):233–238

Ward CA, Balakrishnan A, Hooper FC (1970) On the thermodynamics of nucleation in weak gas–liquid solutions. J Basic Eng Trans 92(4):695–704

Ward CA, Johnson WR, Venter RD, Ho S, Forest TW, Fraser WD (1983) Heterogeneous bubble nucleation and conditions for growth in a liquid–gas system of constant mass and volume. J Appl Phys 54(4):1833–1843

Wilt PM (1986) Nucleation rates and bubble stability in water-carbon dioxide solutions. J Colloid Interface Sci 112(2):530–538

Wong A, Park CB (2012) The effects of extensional stresses on the foamability of polystyrene-talc composites blown with carbon dioxide. Chem Eng Sci 75(1):49–62

Wong A, Leung SN, Li GYG, Park CB (2007) Role of processing temperature in polystyrene and polycarbonate foaming with carbon dioxide. Ind Eng Chem Res 46(22):7107–7116

Wong A, Chu RKM, Leung SN, Park CB, Zong JH (2011) A batch foaming visualization system with extensional stress-inducing ability. Chem Eng Sci 66(1):55–63

Wong A, Guo Y, Park CB, Zhou NQ (2012) Isothermal crystallization-induced foaming of polypropylene under high pressure carbon dioxide. In: 70th annual technical conference of the society of plastics engineers, Orlando, FL. pp 2443–2449

Xu X, Park CB, Xu D, Pop-Iliev R (2003) Effects of die geometry on cell nucleation of PS foams blown with CO_2. Polym Eng Sci 43(7):1378–1390

Yang H–H, Han CD (1984) Effect of nucleating agents on the foam extrusion characteristics. J Appl Polym Sci 29:4465–4470

Zheng WG, Lee YH, Park CB (2010) Use of nanoparticles for improving the foaming behaviors of linear PP. J Appl Polym Sci 117(5):2972–2979